

Synthesis and Characterization of Non-Stoichiometric $\text{Li}_{1.1}\text{Co}_{0.3}\text{Fe}_{2.1}\text{O}_4$ Ferrite Nanoparticles For Humidity Applications

Ebtesam Ateia ElFarhatey (✉ drebtasam2000@yahoo.com)

Cairo University <https://orcid.org/0000-0002-6100-8220>

Mahmoud A. Ateia

Cairo University

M.M. Mosry

Building Physics Institute (BPI)

Charanjeet Singh

Lovely Professional University

M.M. Arman

Cairo University

Research Article

Keywords: Humidity, Nyquist plot, Hopping charge carrier, spinel nanoparticles

Posted Date: November 1st, 2021

DOI: <https://doi.org/10.21203/rs.3.rs-1025245/v1>

License:   This work is licensed under a Creative Commons Attribution 4.0 International License.

[Read Full License](#)

Synthesis and Characterization of non-Stoichiometric $\text{Li}_{1.1}\text{Co}_{0.3}\text{Fe}_{2.1}\text{O}_4$ Ferrite Nanoparticles for Humidity Applications

Mahmoud A. Ateia¹, Ebtessam E. Ateia^{1,2*}, M.M.Mosry³, Charanjeet Singh⁴, M.M. Arman¹

¹ Physics Department, Faculty of Science, Cairo University, Giza, Egypt

² Academy of Scientific Research and Technology (ASRT), Egypt

³ Housing and Building National Research Center (HBRC), Building Physics Institute (BPI), P.O. Box 1770, 87 El-Tahrir St., Dokki, Cairo, Egypt

⁴Department of Electronics, Lovely Professional University, Phagwara, Punjab, India

Abstract:

Humidity sensor plays a crucial role in determining the efficiency of materials and the precision of apparatuses. To measure and control humidity, a non-stoichiometric $\text{Li}_{1.1}\text{Co}_{0.3}\text{Fe}_{2.1}\text{O}_4$ mesopores sensor is synthesized by a modified citrate auto combustion technique.

The XRD study confirms that prepared nanoparticles are cubic spinel structures having Fd3m space group. The crystallite size is approximate 36 nm. Thermal analyses measurements confirm that the samples become thermally stable starting from 600 °C. Additionally, the kinetic studies of the prepared samples are calculated via a pseudo-first-order kinetic model. The temperature dependence of AC conductivity is found to increase with increasing the temperature. These observations are explained in various models. The resistivity mechanism of humidity sensors is studied via Complex impedance spectroscopy (CIS). Its impedance data is fitting to a corresponding circuit, to achieve a simulation of the sample under study. This fitting is detected by the Nyquist plot (Cole-Cole). The obtained data confirms that the studied samples are very sensitive to humidity and can be commercially used as a humidity sensing element.

Keywords: Humidity; Nyquist plot; Hopping charge carrier; spinel nanoparticles;

1. Introduction

Ferrite is an important material, where its structure and physical properties are very favorable at a nanometric scale. It plays a crucial behavior as functional material [1]. Among ferrite nanoparticles, lithium ferrite can be considered as a significant transition metal spinel oxide with the advantage of low price, environmental friendliness, and easy manufacture [2]. The Li ferrite nanoparticles are indexed according to the space group Fd3m [3] and can be characterized as $(\text{A})[\text{B}_2]\text{O}_4$. The “A” and “B” represent the tetrahedral and the octahedral sites respectively [4]. It has been broadly investigated for various applications such as microwave devices and magnetic switching circuits. Additionally, it can be used in lithium batteries.

The effect of cations substitutions on the physical properties of Li nano ferrites is examined by many researchers [5,6]. The reversible loss of lithium and oxygen during the sintering process is the main issue that restricts the

*Corresponding author: drebtessam2000@yahoo.com

preparation process of the lithium ferrites. Therefore, lithium ferrite is often doped with other cations to adjust its physical properties [7].

The nano ferrite is categorized as a high resistivity material. Its resistivity decreases with increasing the surrounding humidity. Spinel ferrite nanoparticles can be used as humidity sensors (HS) due to their high porosity, large surface/volume ratio, high resistivity, low price, and easy preparation [8]. The surrounding humidity can change the resistivity of the ferrite by nearly three orders of magnitude. Generally, the humidity is specified as relative humidity (RH) which signifies the amount of water vapors in the air at a specified temperature. An extensive literature survey reveals a vast majority of sensors are based on ferrite nanoparticles [9].

In this study, the structural, morphological, and electrical properties were performed on $\text{Li}_{1.1}\text{Co}_{0.3}\text{Fe}_{2.1}\text{O}_4$ ferrite nanoparticles. The main challenge is to advance ferrite nanoparticles with high quality, and low cost. These studies offer a good reference value for how to maximize the performances of the examined samples in the HS applications.

2. Experimental Work

2.1. Preparation technique

All chemicals were purchased from Sigma-Aldrich. LiCoFeO_4 was prepared by mixing non- stoichiometric proportions of iron, cobalt, lithium nitrates with the calculated amount of citric acid by citrate auto combustion technique as reported previously [10] with some adjustments as shown in Fig. 1(a,b).

2.2. Device fabrication

Transparent Fluorine doped Tin Oxide (FTO) coated glass substrate has been cleaned to be utilized for sensor fabrication. In brief, a proper amount of sensing material has been grounded carefully in an agate mortar for 10 min, then mixed with a suitable amount of distilled water and grounded again for an additional 10 min to form a past. The slurry was poured on the surface of the pre-cleaned FTO substrate and dried at 60°C for 12hr. Fig. 1(c). illustrates the schematic diagram of the sensor. It was conditioned at 90% RH and AC voltage (1V, 100Hz) for 24 hr to enhance its stability. The behavior and performance of the sensor were evaluated in a homemade humidity-controlled testing chamber as shown in Fig.1:c. More details regarding the humidity testing chamber specifications can be found in our previous work [11].

2.3. Characterization of ferrite nanoparticles

X-ray diffraction (XRD) patterns of ferrite nanoparticles were obtained by an X-ray diffractometer (Xpert PRO MPD) using $\text{CuK}\alpha$ radiation. The shape and size distribution of the nanoparticles were investigated using Field emission scanning electron microscope (FESEM, model Quanta 250). The prepared samples were analyzed through TGA/DTG

with heating rate of 20 °C/min in the temperature range of 25-1000 °C. In addition, the thermodynamic parameters were determined using 1st order reaction rate equation as given in the following relation [12]:

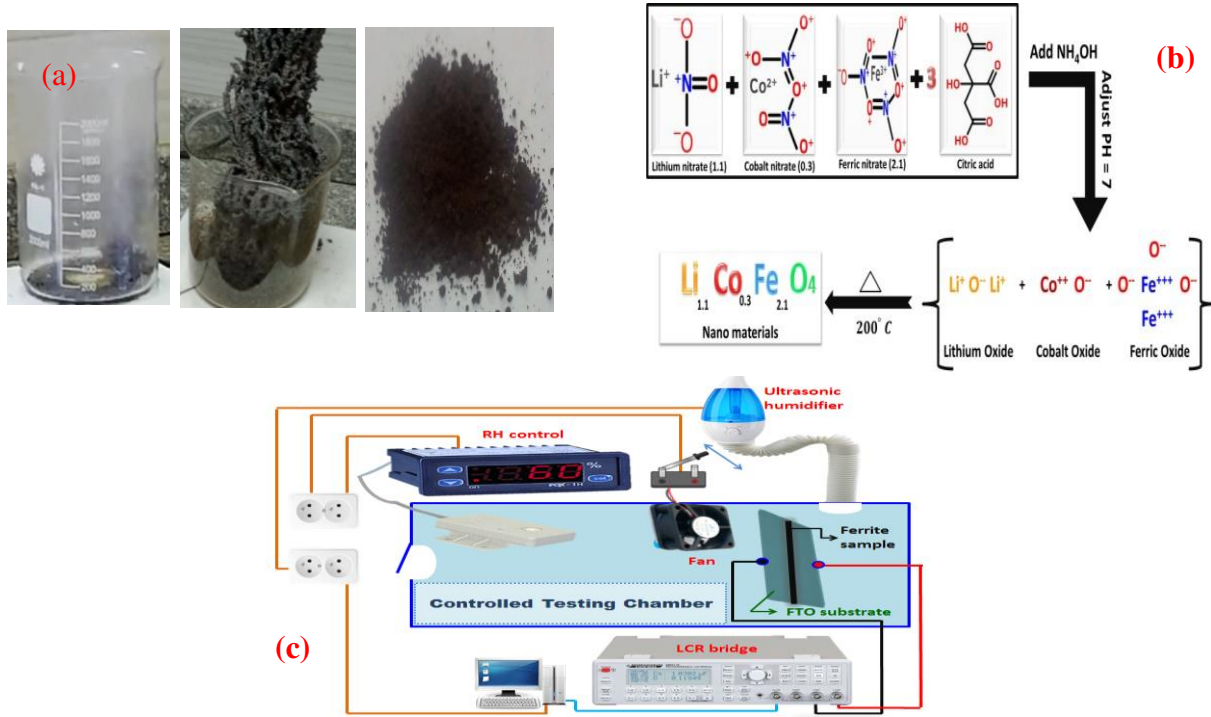


Fig. 1. (a-b) Steps of preparation of $\text{Li}_{1.1}\text{Co}_{0.3}\text{Fe}_{2.1}\text{O}_4$ ferrite nanoparticles. (c) homemade humidity-controlled testing chamber.

$$\frac{dx}{dt} = k(1 - x) \quad (1)$$

$$x = \frac{w_i - w_t}{w_i - w_f} \quad (2)$$

where x is the fracture of sample decomposed at time t , k is rate constant of reaction, w_i is the initial weight, w_f is final weight and w_t is weight of sample at particular time t .

3. Results and Discussion

3.1. structure characterizations

Fig. 2. illustrates the XRD pattern of the $\text{Li}_{1.1}\text{Co}_{0.3}\text{Fe}_{2.1}\text{O}_4$ sample. The obtained data is compared with JCPDS card 04-022-8066.

The formation of a single-phase cubic spinel structure with a space group (Fd-3m) is ratified. The average crystallite size is calculated based on the Debye–Scherrer’s relation as mentioned in the previous work [13]. No additional peaks are detected in the pattern, signifying that $\text{Li}_{1.1}\text{Co}_{0.3}\text{Fe}_{2.1}\text{O}_4$ nanoparticles are completely formed. The value of the lattice parameter (a_{exp}) is estimated using the following relation [14] and tabulated in Table 1.

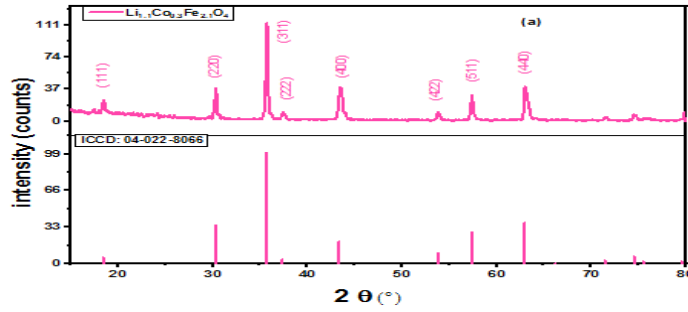


Fig. 2. The XRD diffraction pattern for $\text{Li}_{1.1}\text{Co}_{0.3}\text{Fe}_{2.1}\text{O}_4$.

$$a_{exp} = d\sqrt{h^2 + k^2 + l^2} \quad (3)$$

Where d is the d-spacing and (hkl) are the Miller indices of the planes associated with characteristic peaks.

The X-ray density (D_x), experimental density (d_{exp}), and porosity (P), for $\text{Li}_{1.1}\text{Co}_{0.3}\text{Fe}_{2.1}\text{O}_4$ are demonstrated as mentioned in the previous work [15]. The calculated data is illustrated in the Table 1.

$$d_x = \frac{ZM}{a_{exp}^3 N_A} \quad (4)$$

$$d_B = \frac{m}{\pi r^2 t} \quad (5)$$

$$P(\%) = \left(1 - \frac{d_B}{d_x}\right) \times 100 \quad (6)$$

where Z is number of molecules per unit cell (for spinel ferrites $Z = 8$), M is molecular weight of the sample (g/mole), N_A is the Avogadro's number (6.023×10^{23} atom/mole), and m , r and t are the mass, radius and thickness, respectively, of each pellet of $\text{Li}_{1.1}\text{Co}_{0.3}\text{Fe}_{2.1}\text{O}_4$ nano ferrite sample.

Table 1

The experimental lattice constant (a_{exp}), the theoretical density (d_x), experimental density (d_{exp}), porosity (P) and crystallite size (D) of the investigated sample.

Sample	a_{exp} (Å)	d_x (g/cm ³)	d_{exp} (g/cm ³)	P (%)	D (nm)
$\text{Li}_{1.1}\text{Co}_{0.3}\text{Fe}_{2.1}\text{O}_4$	8.324	4.758	2.528	46.86	36

3.2. Field Emission Scanning Electron Microscope

The FESEM images of the investigated sample are presented in Fig. 3(a-b).

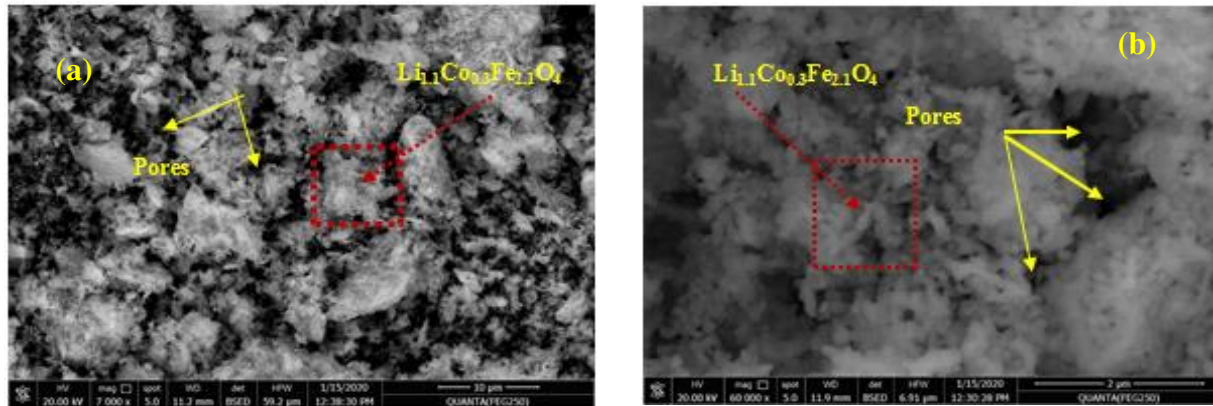


Fig. 3. (a-b) FESEM images of LiCoFeO sample.

The LiCoFeO grains with porous nature and rocky like shape are clearly appeared. As can be seen, the sample is spongy and porous agglomerates. The appearance of porous can be attributed to the escape of gases during the combustion process. The same behavior was attained for copper nano ferrites [16]. The FESEM images show that some of the particles combined with each other to form clusters and leave some spaces as pores. These pores serve as humidity or gas adsorption sites as will be discussed later. The detected porosity from XRD agrees with the FESEM images. The $\text{Li}_{1.1}\text{Co}_{0.3}\text{Fe}_{2.1}\text{O}_4$ with such morphology is highly recommended in humidity sensor applications.

3.3. Thermogravimetric analysis.

Fig. 4(a). shows TGA-DTA plots of the powder in the temperature range 25–1000 °C under N_2 atmosphere. The rate of heating for the process is $20\text{ }^\circ\text{C min}^{-1}$. The TGA plot for the sample is divided into three parts based on various processes taking place in each of them, (i) 30–175 °C (ii) 175–430 °C and (iii) 450–800 °C. The first stage of weight loss WL ($\approx 0.9\text{-}1\text{ }%$) is due to the evaporation of residual water during the preparation technique and represents an exothermic peak (DTG) around 130 °C.

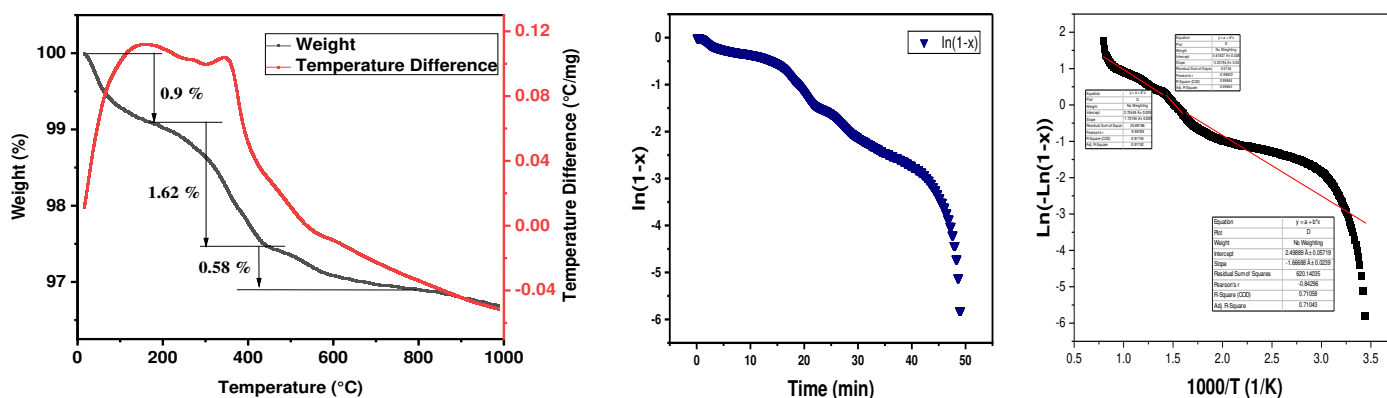


Fig. 4. (a) TGA and DTG for $\text{Li}_{1.1}\text{Co}_{0.3}\text{Fe}_{2.1}\text{O}_4$ ferrite nanoparticle. (b) Plot of $\ln(1-x)$ vs time for Dehydration phase, Decomposition phase and Condensation phase. (c) the relation between $\ln[\ln(1-x)]$ versus $1000/T$.

In the second stage, $\text{WL} \approx (1.6\text{-}2)\text{ }%$ corresponding to the volatilization of the organic solvents and represents an exothermic peak (DTG) around 400 °C.

The third step of the TGA curve is after 600 °C where the WL is in the range of (0.5-0.6) %. This WL may be due to improving the crystallization process of the materials.

The TGA plot shows no further WL above 650 °C, confirming the formation of the stable $\text{Li}_{1.1}\text{Co}_{0.3}\text{Fe}_{2.1}\text{O}_4$ nano ferrite sample. The exothermic peaks in the DTG pattern are consistent with the change regions in the TGA pattern. The kinetic

studies of the prepared samples are calculated via a pseudo-first-order kinetic model. The rate constant (k) can be obtained from the slope of the linear plot of $\ln(1-x)$ against time (t) by using the next equation. The data is plotted in Fig. 4(b).

$$\ln(1-x) = -kt \quad (7)$$

The half-life ($t_{1/2}$) is determined via Eq. (8), and the obtained results are illustrated in Table 2.

$$t_{1/2} = 0.693/k \quad (8)$$

The Coats and Redfern model can be used to detect the kinetics parameters as designated in the following formula [12]:

$$\ln[-\ln(1-x)] = \ln \frac{ART^2}{\beta E_a} - \frac{E_a}{RT} \quad (9)$$

where A , β , and R are the pre-exponential parameter, the heating rate, and the universal gas constant ($8.3143 \text{ Jmol}^{-1} \text{ K}^{-1}$) respectively. While E_a is activation energy and T is the temperature (K). The E_a can be obtained by drawing the relation between $\ln[\ln(1-x)]$ versus $1000/T$ as shown in Fig. 4(c). The E_a values $> 25 \text{ kJ mol}^{-1}$ ratify that this is a chemically controlled reaction and not diffusion or mass transfer limitations. Additionally, other parameters like the change of the entropy (ΔS°), enthalpy (ΔH°), and Gibbs free energy (ΔG°) is calculated using basic thermodynamic equations [17]:

$$\Delta H = E_a - R.T \quad (10) \quad \Delta S = R.\ln\left(\frac{A.h}{K.T}\right) \quad (11) \quad \Delta G = \Delta H - T.\Delta S \quad (12)$$

Where h and K is Blank constant and Boltzmann constant respectively. The results for each phase are tabulated in Table 2. The positive value of ΔH° designates the input heat energy which is required for the reactants. The degree of disturbance of the system can be identified by ΔS . The negative value of ΔS° specifies that the transition state orientation is higher compared to the reactants in the ground state. Additionally, it signifies that the $\text{Li}_2\text{O} + \text{CoO} + \text{FeO}$ join each other to form LiCoFeO which is more organized and stable compared to the ground state and subsequently decreases the randomness of the system. The ΔG gives an idea on, either non-spontaneity or spontaneity of the reaction depending on the +ve or -ve values of ΔG° . In the present study, +ve values of ΔG indicate the non-spontaneous nature of the process.

Table 2

Thermodynamic and Kinetic parameters of each phase during thermogravimetric analysis of $\text{Li}_{1.1}\text{Co}_{0.3}\text{Fe}_{2.1}\text{O}_4$ nanoparticles.

Region (KJmol ⁻¹)	Temp (K)	k (min ⁻¹)	t _{1/2} (min)	E _a (kJmol ⁻¹)	ΔH (kJmol ⁻¹)	ΔS (Jmol ⁻¹ K ⁻¹)	ΔG
First	623	0.034	20.563	18.85	8.67	-284.63	186.0
Second	723	0.137	5.058	25.23	19.22	-265.74	211.3
Third	830	0.107	6.470	14.38	7.48	-289.69	247.9

3.4. Electric properties

The most crucial features of doped nano ferrites are the electrical properties which have a great impact on the enhancement of humidity application

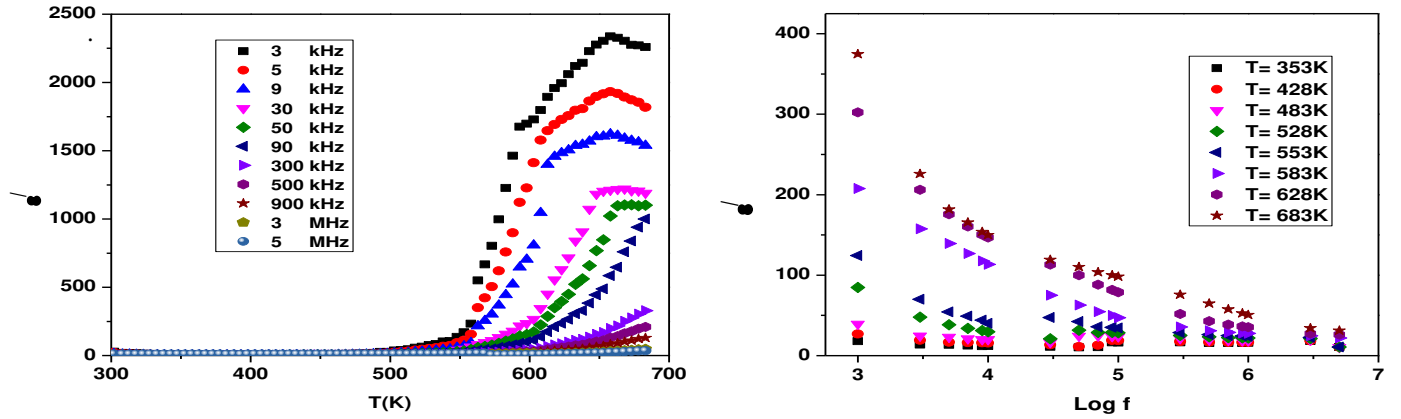


Fig. 5. (a) The dependence of dielectric constant (ϵ') on the absolute temperature as a function of frequency. (b) The dependence of ϵ' on the frequencies.

The dielectric constant (ϵ') gradually increases with increasing temperature till 550 °C then rapidly increases is detected up to 650 °C as shown in Fig. 5 (a-b). The rapid increase in the ϵ' can be attributed to the dipolar polarization. According to Koops' model, ferrites are comprised of two layers, the first is low resistance grains, and the other is high-resistance grain boundaries. When the electric field is applied to the investigated sample, electrons accumulate at grain boundaries and hinders the electron conduction. This accumulation generates space charge polarization. The electron hopping in $\text{Li}_{1.1}\text{Co}_{0.3}\text{Fe}_{2.1}\text{O}_4$ is principally between the elements at B site as Fe^{2+} - Fe^{3+} , and Co^{2+} - Co^{3+} ions [18, 19]. The excess of metals ions in $\text{Li}_{1.1}\text{Co}_{0.3}\text{Fe}_{2.1}\text{O}_4$ (B cations > 2) will greatly increase the probability of electron hopping between Fe^{2+} / Fe^{3+} , and $\text{Co}^{2+}/\text{Co}^{3+}$ ions. This inevitably leads to an increase of space charge reaching the grain boundary, thus increasing the space charge polarization. However, these space charge carriers need some time to line up along their axes by the varying applied field, consequently, ϵ' decreases with increasing frequency.

The relation of $\ln \sigma$ (σ : conductivity) versus the reciprocal of absolute temperature ($1000/T$) at various frequencies is shown in Fig. 6. This plot is fitted for each region to the linear regression line with the appropriate parameter $R2 \approx 0.99$. Additionally, the σ increases with increasing temperature which ratifies the semiconducting-like behavior.

The plot can be divided into three numerous temperature regions corresponding to three various conduction mechanisms. The first is the hopping mechanism that appears below the transition temperature T_c , where the σ is frequency and temperature-dependent. While the second mechanism above T_c is temperature-dependent and frequency- independent. It is related to the drift mobility of the thermally activated electrons and not to the thermal creation of the charge carriers.

In the third region from 603 K to 686 K, the σ is nearly stable with the temperature change. The transition of the investigated sample occurs around 605 K.

The activation energies are estimated from the Arrhenius relation [20] and given in Table 3 at different frequencies. The activation energy for the electron hopping $\text{Fe}^{2+} \leftrightarrow \text{Fe}^{3+}$ is estimated by Rosenberg et al. It is of the order of 0.1 eV. However, the double exchange electron hopping as $\text{Fe}^{2+} + \text{Co}^{3+} \leftrightarrow \text{Fe}^{3+} + \text{Co}^{2+}$ requires more energy for the conduction, and then the

activation energies would naturally be considerably larger. Accordingly, in the present case, the obtained activation energies of the range of 0.2-0.3 eV suggest that the double exchange interaction process is more predominant. The obtained activation energies of pure materials agree well with that reported for the double exchange electron hopping ($\sim 0.25\text{eV}$) [21].

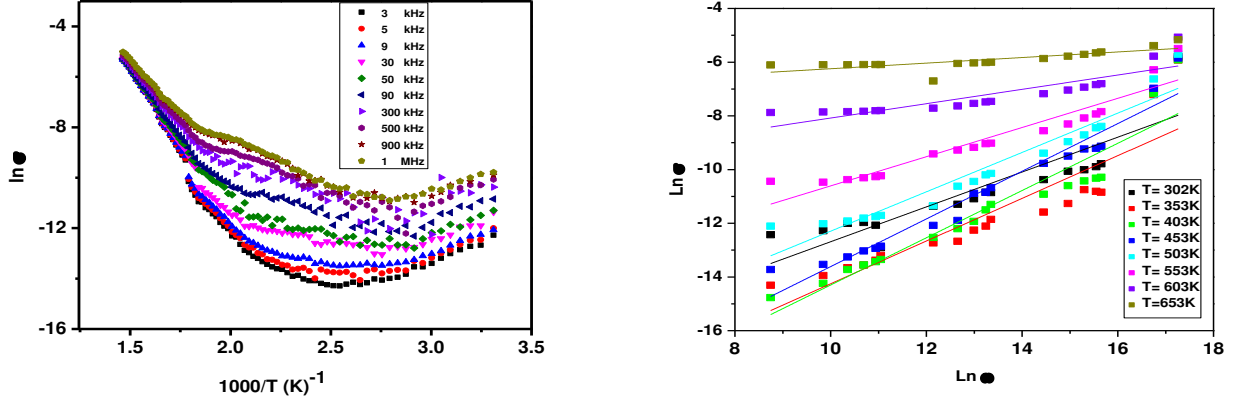


Fig. 6.(a) The relation of $\ln \sigma$ (σ : conductivity) and the reciprocal of absolute temperature ($1000/T$) at different frequencies. (b) The relation of $\ln \sigma$ and $\ln \omega$ for the investigated sample.

Table 3

The activation energies for $\text{Li}_{1.1}\text{Co}_{0.3}\text{Fe}_{2.1}\text{O}_4$.

Frequency (kHz)/ activation energy (eV)	50	90	300	500	900	1000
E_1	0.25	0.21	0.26	0.29	0.30	0.29
E_2	0.98	0.93	0.82	0.77	0.63	0.67

Fig. 6 (b). illustrates the relation of $\ln \sigma$ (σ : conductivity) and $\ln \omega$ (ω : angular frequency) for the sample $\text{Li}_{1.1}\text{Co}_{0.3}\text{Fe}_{2.1}\text{O}_4$ as a function of the absolute temperature. The σ_{ac} obeyed the power law that was discussed previously [22].

$$\sigma_{ac}(\omega) = B \omega^S \quad (13)$$

where σ_{ac} is the ac conductivity, $\omega = 2\pi f$ is the angular frequency, B is a temperature-dependent constant and S is the frequency-dependent exponent. The slope of lines represents the values of the exponent factor (S). The experimental values of the slope S attained for $\text{Li}_{1.1}\text{Co}_{0.3}\text{Fe}_{2.1}\text{O}_4$ is 0.57. The obtained value agrees well with the values (0.6–1.0) found for the hopping mechanism in most transition metal oxide materials [23].

3.5. Humidity sensing studies

The porosity is a significant advantage of nano ferrite which is essential for a humidity sensor. The change of resistivity with exposure to humidity is a basic requirement for the sensor. This change depends on the band gaps, surface morphology, size, diffusion rate of gas, and specific surface area of the used magnetic materials. [24]

The change of the impedance in the frequency range of 100 Hz – 100kHz at RT in a controlled humidity environment from 10- 90 RH% is testified as shown in Fig. 7(a-b). It is observed that the impedance variation decreases with increasing testing frequency. At higher frequencies, this variation is not significant due to the inability of a water molecule to be polarized at higher frequencies [25]. The maximum variation of the impedance is achieved at 100Hz.

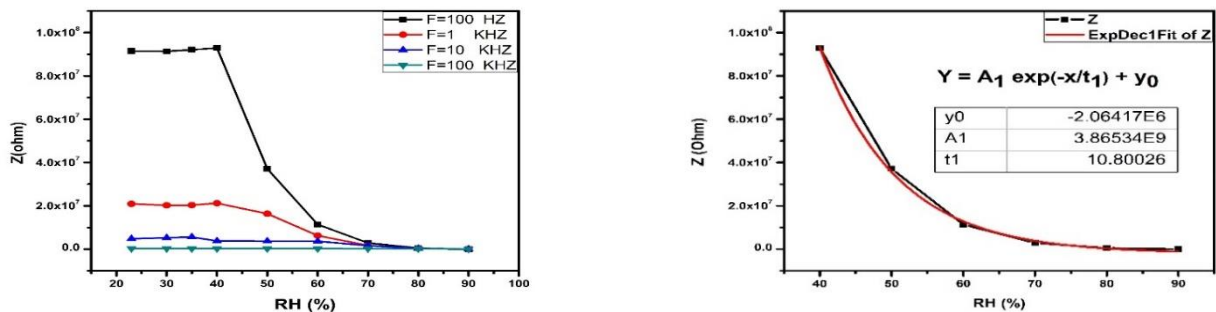


Fig. 7. (a) The impedance of $\text{Li}_{1.1}\text{Co}_{0.3}\text{Fe}_{2.1}\text{O}_4$ versus relative humidity at different frequency. (b) The fitting at 100 Hz.

Consequently, the humidity sensing behavior of $\text{Li}_{1.1}\text{Co}_{0.3}\text{Fe}_{2.1}\text{O}_4$ nanocomposite is evaluated at 100Hz. Additionally, a humidity level lower than 40% is not recommended to be used as humidity sensing for the studied samples. This is clarified by the Physical/Chemical adsorption, of a water molecule on the surface of the sensor.

The humidity sensing behavior of the nanoparticles is elucidated through three consecutive processes including the chemisorptions, the physisorption, and the capillary condensation. Firstly, at low RH values (less than 40%) water molecules (WMs) are chemically adsorbed on the surface of the sensing materials and self-ionized to form H^+ and OH^- . A double hydrogen bond is formed between adsorbed WMs and active sites (e.g. grain boundaries) of sensing materials. Due to the nature of the double hydrogen bond, the proton requires more energy to hop between adjacent OH^- groups [26]. On the other hand, by increasing the RH level, the second layer of WM starts to be physically adsorbed on the active sites of the sensor via a single hydrogen bond. Due to the formation of a single hydrogen bond, the WMs become mobile and behave like those in the bulk liquid. In this manner the amount of ionized WM generates a large number of hydronium ions (H_3O^+) as charge carriers, hence the proton requires less energy for hopping between adjacent WM, thereby decreasing the sensor impedance. This mechanism is known as chain reaction or Grotthuss mechanism [27].

With further increase in RH level, several physisorbed layers are stacked up and the water molecule condenses in the pores causing a further decrease in sensor impedance. The described mechanism is illustrated in Fig. 8.

Hysteresis is one of the most significant experiments required for humidity sensor evaluation. The fabricated sensor is subjected to a controlled humidification/desiccation regime from 40% up to 90% RH and the results are shown in Fig. 9. It is believed that the desorption process is generally slower than the adsorption process, resulting in a change in impedance slightly lower during the desorption than that in the adsorption.

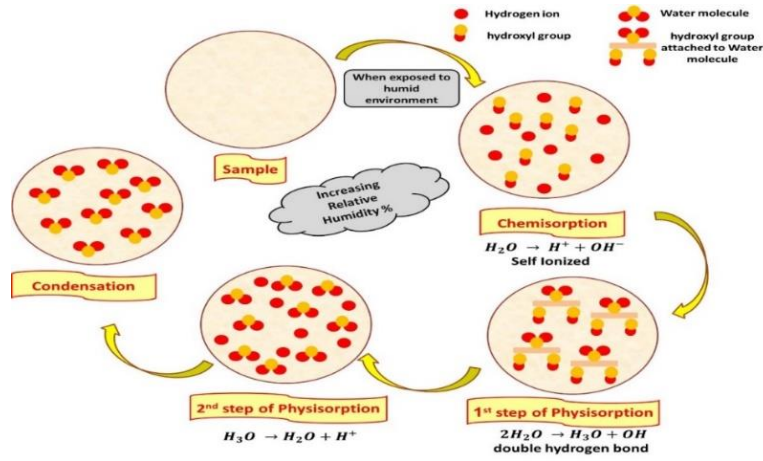


Fig. 8. The mechanism of $\text{Li}_{1.1}\text{Co}_{0.3}\text{Fe}_{2.1}\text{O}_4$ composite as humidity sensing behavior.

The sensor exhibits lower hysteresis and such a humidity sensor is a favor to be integrated into real-time humidity monitoring devices. More importantly, the response of $\text{Li}_{1.1}\text{Co}_{0.3}\text{Fe}_{2.1}\text{O}_4$ displays exponential correlation with increasing RH value from 40 up to 90% as depicted in the figure.

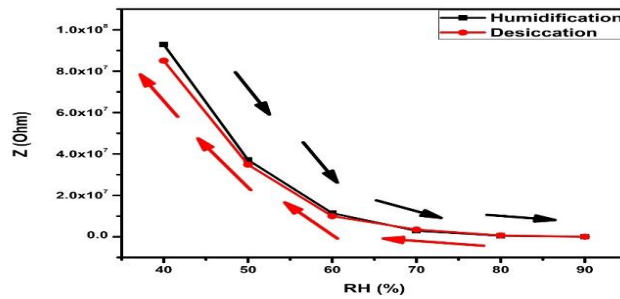


Fig. 9. The hysteresis loop for adsorption and desorption process at 100 Hz and 300K.

The conductivity mechanism of humidity sensors is studied via Complex Impedance Spectroscopy (CIS) [28]. The Nyquist complex impedance curves for $\text{Li}_{1.1}\text{Co}_{0.3}\text{Fe}_{2.1}\text{O}_4$ are estimated over a frequency ranging from 50Hz up to 5 MHz at various humidity levels from 40% up to 90% as shown in Fig. 10: a-d. It is observed that under low humidity circumstances only a nearly straight line can be obtained. With a further increase in humidity level (60% - 70% RH), a semicircle starts to be appearing. By increasing the RH level the curvature of the semicircle decreases due to the interaction between water molecules and the surface of the sensing material. Finally, at a higher level of humidification (80%-90% RH) a semicircle is generated in addition to a straight line at the low-frequency region.

The dissimilarity in impedance curves can be correlated to the different adsorption mechanisms. It is well known that the semicircle in the CIS curves characterizes the intrinsic impedance of the sensing material. While the line at low frequency represents the Warburg impedance [29]. In low humidity conditions, only a few water molecules are adsorbed on the surface of the sensing material and a semicircle or incomplete semicircle appears in the CIS curve, thereby restricting the movement of the charge carrier. Further increasing of humidity level, the Warburg impedance is dominant which implies that a continuous water layer is formed on the surface of the sensing material and hence the

ionic conduction occurs. Additionally, the CIS of the investigated sample is depending on an idealized circuit model with various electrical components. Its impedance data is fitting to a corresponding circuit, to achieve a simulation of the sample under study. This fitting is detected by the Nyquist plot (Cole-Cole). The equivalent circuit is illustrated in the inset of Fig. 10: c,d. The electric circuit elements have been attained using Z view software.

Finally, the obtained data clarify that $\text{Li}_{1.1}\text{Co}_{0.3}\text{Fe}_{2.1}\text{O}_4$ nano ferrites are containing two phases; the grain and grain boundary. Also, approve that the interpretation of the behavior of dielectric parameters and conductivity is on the correct track.

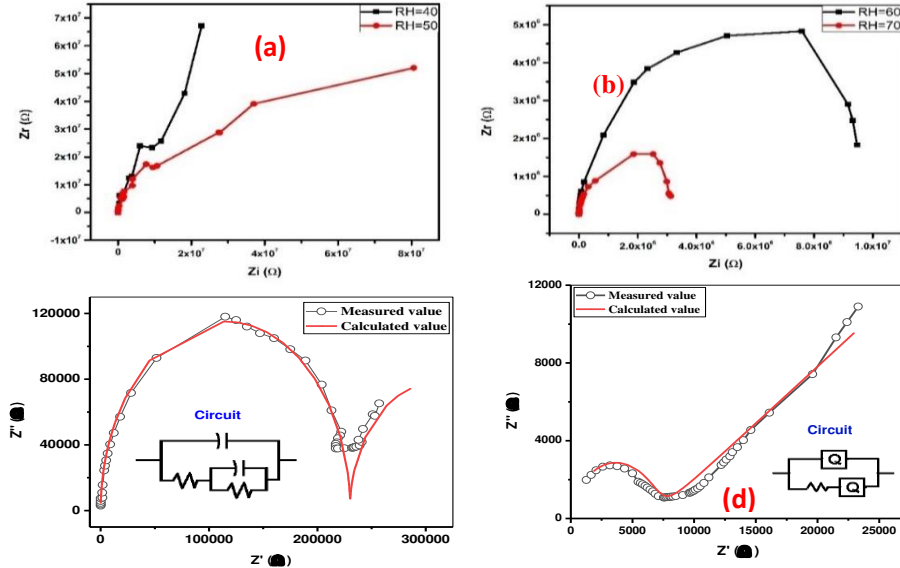


Fig. 10. (a) The Nyquist complex impedance curves for $\text{Li}_{1.1}\text{Co}_{0.3}\text{Fe}_{2.1}\text{O}_4$ at RH (40 :50) % . (b) at RH (60 : 70) % . (c) at RH (80) % . (d) at RH (90) % at room temperature.

4. Conclusion

The magnetic nano particles $\text{Li}_{1.1}\text{Co}_{0.3}\text{Fe}_{2.1}\text{O}_4$ was synthesized in a single-phase cubic spinel structure using citrate auto combustion technique. The FESEM images illustrated the porous nature and rocky like shape of the sample. The main conduction mechanism is the electron hopping between the elements at B site as Fe^{2+} - Fe^{3+} , and Co^{2+} - Co^{3+} ions. The maximum impedance value is achieved at 100Hz; therefore, the humidity sensing behavior of $\text{Li}_{1.1}\text{Co}_{0.3}\text{Fe}_{2.1}\text{O}_4$ is evaluated at 100Hz. The humidity sensing behavior of the nanoparticles has two mechanisms; the chemisorptions at low RH values and the physisorption at high RH value. The increase of the RH level decreases the curvature of the semicircle due to the interaction between water molecules and the surface of the sensing material.

Author's contribution

Ebtesam E. Ateia: Experimentation, written the original manuscript, reviewing and editing the final manuscript, supervision

Mahmoud A. Ateia: Material preparation, data collection and analysis, Optimum selection of material parameters, Experimentation, Validation and Visualization.

Mohamed M. Mosry: Experimentation, and written the original manuscript.

Charanjeet Singh: Validation, and, Visualization

Mohamed . M. Arman: Conceptualization, Investigation; Experimentation, Review and editing.

Funding

This research was funded by Academy of Scientific Research & Technology (No. 6722)

Acknowledgments

This paper is supported financially by the Academy of Scientific Research and Technology (ASRT), Egypt, under initiatives of Science Up Faculty of Science (Grant No. 6722).

Conflict of interest:

The authors declare that there is no conflict of interest in this work.

References

- [1] R. Cheruku, G. Govindaraj, L. Vijayan, Super-linear frequency dependence of ac conductivity in nanocrystalline lithium ferrite, *Mater. Chem. Phys.* 146, 389–398(2014), <https://doi.org/10.1016/j.matchemphys.2014.03.043>.
- [2] N. Rezlescu, C. Doroftei, E. Rezlescu, and P. D. Popa, *Sensors Actuators B Chem.* 133, 420 (2008), <https://doi.org/10.1016/j.snb.2008.02.047>.
- [3] H.M. Widatallah, C. Johnson, F.J. Berry, E. Jartych, A.M. Gismelseed, M. Pekala, On the synthesis and cation distribution of aluminum-substituted spinel-related lithium ferrite, J. Grabski, *Mater. Lett.* 59 (2005) 1105–1109, <https://doi.org/10.1016/j.matlet.2004.12.017>.
- [4] J.V. Angadi, A.V. Anupama, R. Kumar, H.K. Choudhary, S. Matteppanavar, H.M. Somashekarappa, B. Rudraswamy, B. Sahoo, Composition dependent structural and morphological modifications in nanocrystalline Mn-Zn ferrites induced by high energy gamma-irradiation, *Mater. Chem. Phys.* 199 (2017)313e321, <https://doi.org/10.1016/j.matchemphys.2017.07.021>.
- [5] B.K. Kuanr, Effect of the strong relaxor cobalt on the parallel and perpendicular pumping spin-wave instability threshold of LiTi ferrites, *J. Magn. Magn. Mater.* 163(1996)164–172, [https://doi.org/10.1016/S0304-8853\(96\)00306-X](https://doi.org/10.1016/S0304-8853(96)00306-X).
- [6] Mathew George, Swapnaw S. Nair, Asha Mary John, P. A. Joy, M. R. Anantharaman, Structural, magnetic and electrical properties of the sol-gel prepared $\text{Li}_{0.5}\text{Fe}_{2.5}\text{O}_4$ fine particles, *J. Phys. D: Appl. Phys.* 39(2006)900–910, <http://dyuthi.cusat.ac.in/purl/4349>.
- [7] L. P. Babu Reddy *et al.*, “Copper ferrite-yttrium oxide (CFYO) nanocomposite as remarkable humidity sensor,” *Inorganic Chemistry Communications*, vol. 99, no. October 2018, pp. 180–188, 2019, <https://doi.org/10.1016/j.inoche.2018.11.024>.
- [8] I. Soibam, S. Phanjoubam, C. Prakash, Magnetic and Mossbauer studies of Ni substituted Li–Zn ferrite, *J. Magn. Magn. Mater.* 321 (2009) 2779–2782, <https://doi.org/10.1016/j.jmmm.2009.04.011>.
- [9] E. E. Ateia , M. M. Arman, M. Morsy, Synthesis, characterization of NdCoO_3 perovskite and its uses as humidity sensor, *Applied Physics A* (2019) 125:883, <https://doi.org/10.1007/s00339-019-3168-6>.

- [10] E. E. Ateia, "Assessing of channel structure and magnetic properties on heavy metal ions removal from water," *J. Mater. Sci. Mater. Electron.*, 2021, doi: 10.1007/s10854-021-07008-9, <https://doi.org/10.1007/s10854-021-07008-9>.
- [11] E. E. Ateia and A. T. Mohamed, "Humidity sensor applications based on mesopores - LaCoO₃," *Journal of Materials Science: Materials in Electronics*, vol. 30, no. 21, pp. 19254–19261, 2019, <https://doi.org/10.1007/s10854-019-02284-y>.
- [12] M. A. Farrukh, K. M. Butt, K. K. Chong, and W. S. Chang, "Photoluminescence emission behavior on the reduced band gap of Fe doping in CeO₂-SiO₂ nanocomposite and photophysical properties," *J. Saudi Chem. Soc.*, vol. 23, no. 5, pp. 561–575, 2019, doi: 10.1016/j.jscs.2018.10.002, <https://doi.org/10.1016/j.jscs.2018.10.002>.
- [13] E. E. Ateia, M. K. Abdelmaksoud, and H. Ismail, "A study of the magnetic properties and the magneto-crystalline anisotropy for the nano-composites CoFe₂O₄/Sm_{0.7}La_{0.3}FeO₃," *J. Mater. Sci. Mater. Electron.*, vol. 32, no. 4, pp. 4480–4492, 2021, doi: 10.1007/s10854-020-05189-3, <https://doi.org/10.1007/s10854-020-05189-3>.
- [14] Lakshita . PHOR, Vinod KUMAR, Structural, thermomagnetic, and dielectric properties of Mn_{0.5}Zn_{0.5}Gd_xFe_{2-x}O₄ (x = 0, 0.025, 0.050, 0.075, and 0.1). *Journal of Advanced Ceramics* 2020, 9(2): 243-254, <https://doi.org/10.1007/s40145-020-0364-y>.
- [15] M.A. Ahmed, M. Solyman Selim, M.M. Arman, Novel multiferroic La_{0.95}Sb_{0.05}FeO₃ orthoferrite, *Materials Chemistry and Physics* 129 (2011) 705– 712, <https://doi.org/10.1016/j.matchemphys.2011.03.033>.
- [16] Xuan Zhao, Yue Fu, Jin Wang, Yujiao Xu, Jing-Hua Tian, Ruizhi Yang, Ni-doped CoFe₂O₄ Hollow Nanospheres as Efficient Bi-functional Catalysts, *Electrochimica Acta* 201 (2016) 172–178, <https://doi.org/10.1016/j.electacta.2016.04.001>
- [17] S. K. Paswan *et al.*, "Optimization of structure-property relationships in nickel ferrite nanoparticles annealed at different temperature," *J. Phys. Chem. Solids*, vol. 151, no. October 2020, p. 109928, 2021, doi: 10.1016/j.jpcs.2020.109928, <https://doi.org/10.1016/j.jpcs.2020.109928>.
- [18] G.A. Sawatzky, F. VAN DER Woude, A.H. Morrish, Cation Distributions in Octahedral and Tetrahedral Sites of the Ferrimagnetic Spinel CoFe₂O₄, *J. Appl. Phys.* 39 (1968) 1204-1205, <https://doi.org/10.1063/1.1656224>.
- [19] R. Yadav, M.K. Yadav, N.K. Singh, Electrocatalytic Properties of Sol-Gel Derived Spinel Co_xFe_{3-x}O₄ (0 ≤ x ≤ 1.5) Electrodes for Oxygen Evolution in Alkaline Solution, *Int. J. Electrochem. Sci.* 8 (2013) 6321–6331, <http://electrochemsci.org/papers/vol8/80506321.pdf>.
- [20] Jin Soo Kim, Hai Joon Lee, Sun Young Lee, Ill Won Kim, Su Dae Lee, Frequency and temperature dependence of dielectric and electrical properties of radio-frequency sputtered lead-free K_{0.48}Na_{0.52}NbO₃ thin films, *The Solid Films* 518 (2010) 6390 – 6393, <https://doi.org/10.1016/j.tsf.2010.02.078>.
- [21] B. Senthilkumar, R. Kalai Selvan, P. Vinothbabu, I. Perelshtein, and A. Gedanken, "Structural, magnetic, electrical and electrochemical properties of NiFe₂O₄ synthesized by the molten salt technique," *Mater. Chem. Phys.*, vol. 130, no. 1–2, pp. 285–292, 2011, doi: 10.1016/j.matchemphys.2011.06.043, <https://doi.org/10.1016/j.matchemphys.2011.06.043>.
- [22] S. Singh, S. C. Katyal, and N. Goswami, "Dielectric and electrical study of zinc copper ferrite nanoparticles prepared by exploding wire technique," *Appl. Phys. A Mater. Sci. Process.*, vol. 125, no. 9, pp. 1–14, 2019, doi: 10.1007/s00339-019-2936-7, <https://doi.org/10.1007/s00339-019-2936-7>.

- [23] A.S. Das, M. Roy, D. Biswas, R. Kundu, A. Acharya, D. Roy, S. Bhattacharya, Ac conductivity of transition metal oxide doped glassy nanocomposite systems: temperature and frequency dependency. *Mater. Res. Express*. 5, 095201 (2018), *Materials Research Express*, Volume 5, Number 9.
- [24] E. Rios, J.L. Gautier, G. Poillerat, P. Chartier, Mixed valency spinel oxides of transition metals and electrocatalysis: case of the $M_nxCo_{3-x}O_4$ system, *Electrochim. Acta* 44 (1998) 1491–1497, [https://doi.org/10.1016/S0013-4686\(98\)00272-2](https://doi.org/10.1016/S0013-4686(98)00272-2).
- [25] M. Morsy, M. M. Mokhtar, S. H. Ismail, G. G. Mohamed, and M. Ibrahim, “Humidity Sensing Behaviour of Lyophilized rGO/Fe₂O₃ Nanocomposite,” *Journal of Inorganic and Organometallic Polymers and Materials*, vol. 30, no. 10, pp. 4180–4190, 2020, <https://doi.org/10.1007/s10904-020-01570-1>.
- [26] A. Tripathy *et al.*, “Design and development for capacitive humidity sensor applications of lead-free Ca, Mg, Fe, Ti-oxides-based electro-ceramics with improved sensing properties via physisorption,” *Sensors (Switzerland)*, vol. 16, no. 7, 2016, <https://doi.org/10.3390/s16071135>.
- [27] P. Chavan, “Chemisorption and Physisorption of Water Vapors on the Surface of Lithium-Substituted Cobalt Ferrite Nanoparticles,” *ACS Omega*, vol. 6, no. 3, pp. 1953–1959, 2021, doi: 10.1021/acsomega.0c04784, <https://doi.org/10.1021/acsomega.0c04784>.
- [28] T. Şaşmaz Kuru, M. Kuru, and S. Bağcı, “Structural, dielectric and humidity properties of Al-Ni-Zn ferrite prepared by co-precipitation method,” *Journal of Alloys and Compounds*, vol. 753, pp. 483–490, 2018, <https://doi.org/10.1016/j.jallcom.2018.04.255>.
- [29] X. Zhao, X. Chen, X. Yu, X. Ding, X. L. Yu, and X. P. Chen, “Fast response humidity sensor based on graphene oxide films supported by TiO₂ nanorods,” *Diamond and Related Materials*, vol. 109, no. April, p. 108031, 2